

# Improved Physics-Based Simulation of the LEO Space Environment

Eric K. Sutton<sup>1</sup>, Marcin D. Pilinski<sup>2</sup>, Shaylah M. Mutschler<sup>3</sup>, Jeffrey P. Thayer<sup>1,3</sup>,  
Thomas E. Berger<sup>1</sup>, Vu Nguyen<sup>4</sup>, Dallas Masters<sup>4</sup>

<sup>1</sup>*Space Weather Technology, Research and Education Center (SWx TREC),  
University of Colorado at Boulder*

<sup>2</sup>*Laboratory for Atmospheric and Space Physics (LASP), University of Colorado at Boulder*

<sup>3</sup>*Ann and H.J. Smead Aerospace Engineering Sciences, University of Colorado at Boulder*

<sup>4</sup>*Spire Global, Inc., Boulder, CO*

## 1. ABSTRACT SUMMARY

Satellite-Atmosphere interactions cause large uncertainties in low-Earth orbit determination and prediction. Thus, knowledge of and the ability to predict the space environment, most notably thermospheric mass density, are essential for operating satellites in this domain. Recent progress has been made toward supplanting the existing empirical, operational methods with physics-based data-assimilative models by accounting for the complex relationship between external drivers and their response in the upper atmosphere. Simultaneously, a new era of CubeSat constellations is set to provide data with which to calibrate our upper-atmosphere models at higher resolution and cadence. This paper details efforts to combine assimilative methods with new information provided by CubeSats.

## 2. INTRODUCTION AND BACKGROUND

Within low-Earth orbit (LEO), a region spanning roughly 100 to 1000 km in altitude for the purposes of this paper, interactions between man-made satellites and the ambient atmosphere cause large uncertainties in the orbit determination and prediction processes. During episodic periods of moderate to severe space weather activity, such atmospheric drag uncertainties can amplify by a factor of 2–5 in a matter of minutes to hours [1,2]. These uncertainties, when combined with the steadily growing launch rate of small satellites and CubeSats and our advancing ability to track smaller and smaller objects, are poised to overwhelm the U.S. Department of Defense infrastructure currently carrying out the Detect–Track–Catalog mission. Products of this mission are pervasive across the Space Domain Awareness (SDA) enterprise and form a critical infrastructure for nearly all space-based activities. Thus, knowledge and prediction of the space environment, particularly the neutral mass density of the thermosphere and lower exosphere, are an essential part of satellite operations within LEO.

One of the major obstacles in predicting orbit trajectories hours to days in advance, and in correlating consecutive or irregular object tracks, comes from the legacy framework used to model the upper atmosphere’s state and its interaction with satellites and debris. The current model employed by the Combined Space Operations Center (CSpOC) is the High Accuracy Satellite Drag Model (HASDM) [3], an empirical model that self-calibrates by ingesting ground-based tracking data of a select set of orbiting “calibration objects”—i.e., operational and defunct satellites passing through LEO with reasonably stable ballistic coefficients. While this method provides an accurate global-average snapshot of the upper atmosphere, its abilities to capture realistic spatial structure and forecast into the future are limited. Physics-based upper atmosphere simulation approaches offer a vast potential improvement in this regard. Models in this category solve a set of Navier-Stokes fluid equations that have been appropriately tailored for use in the upper atmosphere and are therefore inherently better equipped for simulating a dynamic system response to impulsive energy input from the solar wind. The primary reason such physics-based methods have not been adopted by operational centers to date is the lack of robust data assimilation schemes capable of self-calibrating at levels equal to or better than those currently used in combination with empirical models.

Fortunately, significant strides have been made in recent years toward supplanting empirical methods with physics-based data assimilative models of the upper atmosphere. One such advancement has been accomplished by accounting for the complex relationship between external drivers—namely solar flux and geomagnetic heating—and the response of the upper atmosphere by employing a new least-squares filter called the Iterative Driver Estimation and Assimilation (IDEA) technique [4]. The new filter operates similarly to an unscented Kalman filter (UKF) with the addition of mechanisms to accommodate the lagged response of the upper atmosphere to variations in the external drivers. Using this new technique, notable improvements in spatial accuracy have already been demonstrated [4],

which can help to lower uncertainty across the LEO catalog and increase the efficiency of Space Traffic Management (STM) activities. In addition, the emergence of large constellations of commercial and academic CubeSats over the past 5 years brings with it an excellent opportunity. Most newer SmallSats and CubeSats are equipped with Global Navigation Satellite System (GNSS) devices, making them excellent sources of Precision Orbit Determination (POD) information. Many are also equipped with the ability to monitor their attitude, allowing the construction of an accurate force model. These two pieces of information can be combined to initialize and constrain models of the upper atmosphere.

When compared with conventional observations from ground-based radar tracks of known objects, such as those ingested by HASDM, satellite-based GNSS observations are capable of describing the space environment at a much higher spatial resolution and temporal cadence. Whereas the conventional radar-derived, satellite-drag data sets operate on a multi-orbit to multi-day cadence, we will show that the GNSS-derived data sets are capable of operating at a cadence of a single orbit. Even higher cadences may also be possible but will require further development. The remainder of the paper details our efforts to use the new set of information provided by CubeSats to drive a physics-based, data-assimilative approach to simulating atmospheric densities in LEO.

### 3. METHODS, ASSUMPTIONS, AND PROCEDURES

#### 3.1 Datasets

Spire operates a constellation of over 80 CubeSats in LEO with altitudes ranging from 400–650 km and inclinations spanning the globe, from equatorial to polar orbits (see Fig. 1).

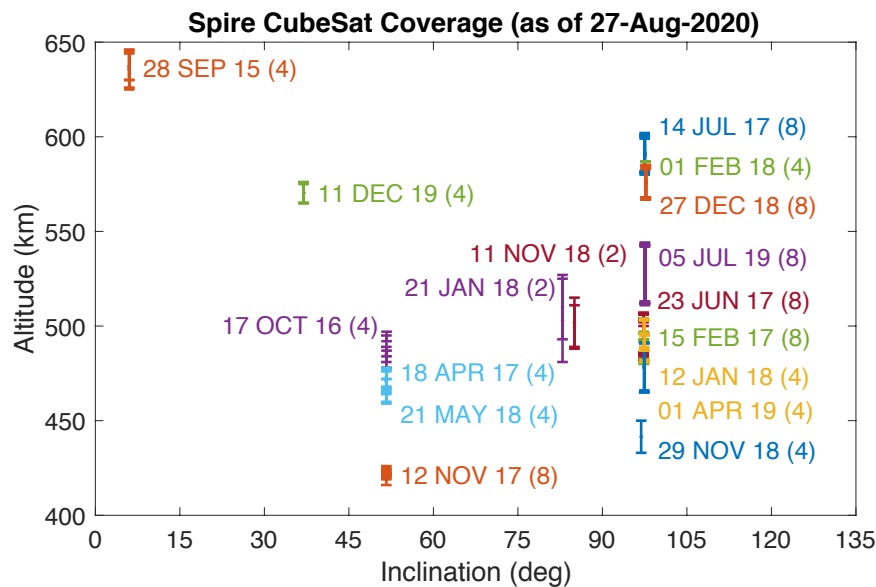


**Fig. 1.** Current coverage of altitude versus inclination for the Spire constellation of CubeSats (as of 27 Aug. 2020). The error bars show the perigee-to-apogee range of altitudes. CubeSats are color coded by common launch dates with the total number of CubeSats in each launch group labeled in parentheses.

The data sets used in this study were provided by Spire Global as part of the NASA Commercial SmallSat Data Pilot Program and cover the period of 23 Sept.–9 Dec. 2018. For the purposes of our work, the following data products were utilized:

- Precision Orbit Determination (POD) solution ephemeris derived from GNSS tracking
- Satellite pointing in the form of attitude quaternions
- Satellite geometry model

POD solutions were typically available during the duty cycle of the GNSS/Radio Occultation (RO) instrument. For the 2018 dataset, duty cycles were in the range of 30–40% of the time, usually concentrated along 40- to 60-minute segments of an orbit (referred to as an orbit arc hereafter). This efficiency has increased with more recent CubeSat builds such that current duty cycles are beginning to approach 100%. For the current data set, ephemeris from each

orbit arc were estimated using the RTOrb software ([https://gps-solutions.com/brochures/GPSS\\_Brochure\\_RTOrb\\_Nov\\_2011.pdf](https://gps-solutions.com/brochures/GPSS_Brochure_RTOrb_Nov_2011.pdf)). This software implements a Kalman filter-based approach to estimate orbit ephemeris. As configured for the current dataset, RTOrb considers Earth’s gravity up to degree and order 120 from the EIGEN-2 model [5], Luni-Solar 3<sup>rd</sup> body perturbations, atmospheric drag assuming densities from the Mass Spectrometer Incoherent Scatter extension (MSISE-90) model [6], and solar radiation pressure (SRP) with cylindrical Earth-shadowing effects. The latter two effects use a cannonball approach in which coefficients of drag and reflectivity are estimated within each arc, respectively, along with the orbit ephemeris. The treatment of drag and SRP in the POD process is not to be confused with the force model described later in this section; instead, the parameters estimated here have little bearing on our calculations of orbit energy.

The attitude of the Spire CubeSats is represented by a quaternion describing the transformation from the body-fixed coordinate system (see Figure 4 below) to the vehicle velocity/local horizontal (VVLH) orbit-based coordinate system at a given instance in time. In the initial phases of the NASA Data Pilot assessment, quaternions were provided at an approximate cadence of 10 seconds during the duty cycle of the GNSS/RO receiver, with nothing available outside of the duty cycle. However, it was realized early on in the project that, due to frequent orientation maneuvers, the accuracy of the retrieved neutral densities would be limited by any breaks in continuity of satellite attitude data (see Section 3.3 for further details). The attitude mode of the CubeSats frequently switched between an observing mode aligning GNSS/RO antennas along track and a mode that maximizes the amount of solar flux incident on the solar panels. Because these changes in orientation modify the integrated effect that atmospheric drag has on the orbit parameters, the orientation must be monitored constantly in order to convert orbital energy loss rates to an atmospheric density. Spire has since updated their processing chain for the entire fleet to ensure that a continuous stream of attitude quaternions is available for any datasets originating after 2018. However, for the 2018 data set, we limited processing to a small subset of three CubeSats from Spire Global’s constellation for which attitude data had been continuously downlinked and archived. These satellites, which will be used throughout the remainder of the paper, are referred to by Spire’s internal satellite ID numbers: 83, 84, and 85. These three CubeSats trace back to a common launch on 21 May 2018 into a 51.6° inclination orbit. During the time period of interest these satellites orbited between the altitudes of 467–492 km. Additional properties and designations of these CubeSats can be found in Table 1.

Table 1. Properties of Spire CubeSats used in this study

Spire ID	NORAD ID	COSPAR ID	Perigee/Apogee Altitude (km)	Inclination (degrees)	S/C Mass (g)
83	43560	2018-046G			
84	43559	2018-046F	467–492	51.6	4933 ± 4
85	43558	2018-046E			

Fig. 2 shows the geometry for the three Spire CubeSats. The GNSS/POD antenna nominally points in the zenith direction while the front radio occultation (FRO) antenna generally points along the in-track or anti-in-track directions when the satellite is recording RO data. When the RO instrument is cycled off, the satellite reorients in such a way as to maximize illumination of the solar panels.

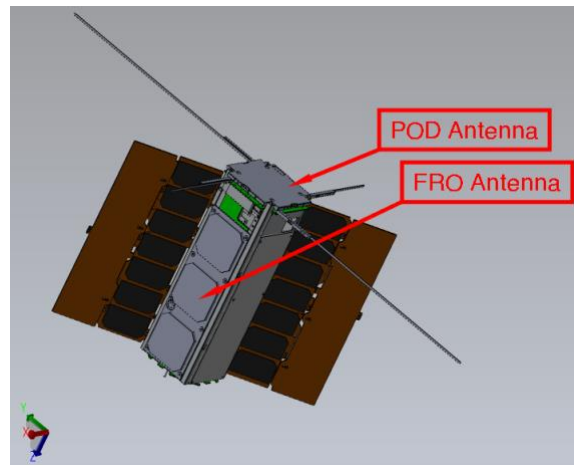


Fig. 2. Computer model of Spire’s version 3.3 Lemur CubeSat.

### 3.2 Observation Processing

To drive our data assimilative process, we use information from GNSS measurements taken aboard CubeSats. There are several methods available to infer neutral densities from orbit positioning information. For instance, this can be done by estimating a scaling correction for a density model within a POD solution, e.g., [7]. We choose instead to employ an energy tracking method that uses the existing POD solutions routinely obtained by Spire. The first step is to calculate the orbital energy at each available ephemeris data point and track the change in this quantity between subsequent orbits. For an Earth-orbiting satellite, this energy can be approximated in the following way:

$$\xi = \frac{v^2}{2} - \omega_{Earth}^2 \frac{x^2+y^2}{2} - \frac{\mu}{r} + U_{nonSpherical} \quad (1)$$

where  $r = \sqrt{x^2 + y^2 + z^2}$  and  $v$  are the satellite's respective position and velocity in an Earth-centered Earth-fixed (ECEF) coordinate frame,  $\omega_{Earth}^2$  is the rotation rate of the Earth,  $\mu$  is the gravitational parameter for the Earth, and  $U_{nonSpherical}$  is a potential function composed of the non-spherical terms of Earth's gravity. In the absence of nonconservative forces (e.g., atmospheric drag or solar radiation pressure) or any additional perturbing conservative forces (e.g., 3rd body attraction, solid Earth tides, ocean tides, atmospheric tides, etc.),  $\xi$  is a conserved quantity along the orbit of a satellite.

We have found that the choice of ECEF coordinates becomes important when non-spherical gravity terms are considered, particularly any non-zonal terms (i.e., order  $m > 0$ ). In ECEF coordinates,  $U_{nonSpherical}$  is clearly a function of position alone. The alternate formulation of the energy equation in an inertial coordinate frame, however, would require  $U_{nonSpherical}$  to be a function of both position and time, violating the assumptions underlying a potential function and its use in the energy equation. As a result, the formulation of energy in an inertial coordinate frame does not remain constant along an orbit when considering non-zonal terms—even in the absence of nonconservative forces—and leads to twice-daily oscillations of approximately  $\pm 130$ – $140$  J/kg/s or  $m^2/s^3$  for the orbits analyzed in this paper, or equivalently, about  $\pm 30$ – $35$  m in the semi-major axis. Much of this can be directly attributed to the  $n = m = 2$  gravitational potential term, which is the largest non-zonal term in  $U_{nonSpherical}$ .

If we describe the Earth's gravity field using the two-body approximation—ignoring for a moment the non-spherical contribution—the energy dissipation due to atmospheric drag remains obscured by the large variations in energy due to the  $J_2$  and higher-order gravitational terms. Fig. 3 shows this simplified calculation of orbital energy for a single CubeSat from Spire Global's constellation during the period spanning 23 Sept.–9 Dec. 2018. In this plot, color coding is used to enable the visual distinction of adjacent days.

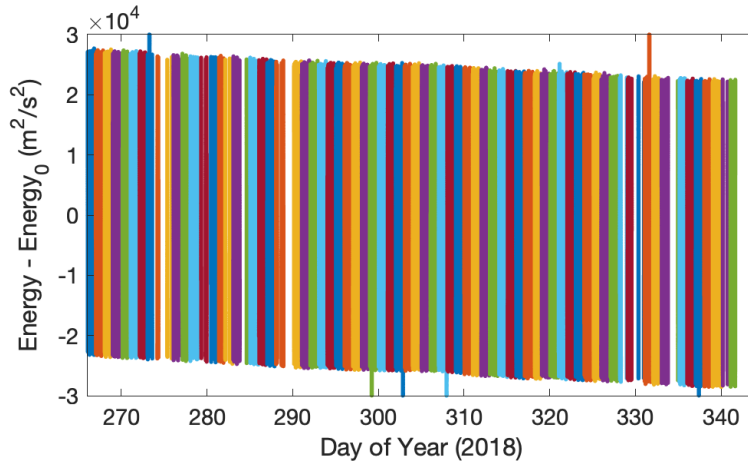


**Fig. 3.** Keplerian orbital energy (i.e., ignoring the  $U_{nonSpherical}$  term from Eq. 1) for Spire CubeSat 83 during the period of 23 Sept.–9 Dec. 2018. Color coding is used here to enable the visual distinction of adjacent days.

However, when we account for a  $36 \times 36$  spherical harmonic gravity field, the change in energy caused by atmospheric drag is more readily isolated from variations in the gravity field. Fig. 4 depicts the orbital energy of the three CubeSats over the same time span as Fig. 3. To conform with the POD solutions, we use the non-spherical terms from the

EIGEN-2 gravity model [5]. We found that, for our purposes, including terms above a 36x36 expansion yielded diminishing returns.

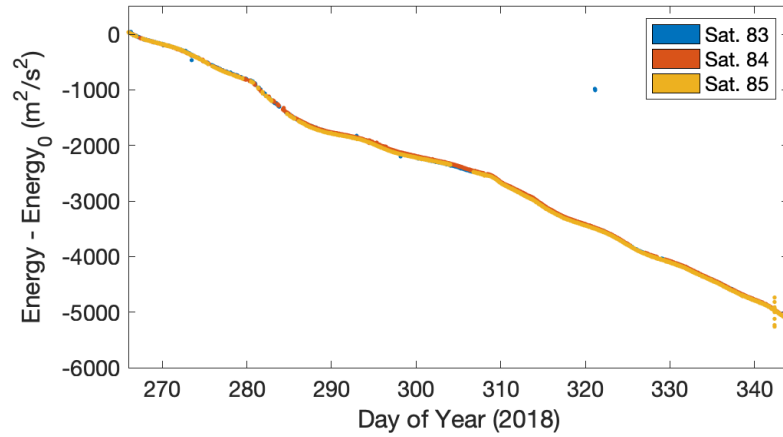


**Fig. 4.** Orbital energy (i.e., including the  $U_{nonSpherical}$  term from Eq. 1) for Spire CubeSats 83, 84, and 85 during the period of 23 Sept.–9 Dec. 2018.

Changes in energy were on the order of 5000 m<sup>2</sup>/s<sup>2</sup> over the entire period of analysis, or about 65 m<sup>2</sup>/s<sup>2</sup> per day. This is equivalent to a change in the semi-major axis of 1.2 km total, or about 15 meters per day. After applying a simple filter to reject erroneous arcs (note the obvious outliers on day 273, 320, and 342 in Fig. 4), the noise level of these timeseries of orbital energy is now low enough to derive an effective energy dissipation rate between subsequent orbit arcs.

### 3.3 Force Model

To interpret the timeseries of energy from Fig. 4 in terms of the behavior of the upper atmosphere, it is necessary to understand how the satellite drag interaction depends on atmospheric density. The rate at which energy is lost from a satellite's orbit to the atmosphere via the drag force, or the energy dissipation rate (EDR), can be related to atmospheric mass density through the following equation:

$$EDR \equiv -\frac{d\xi}{dt} = \frac{1}{2m} C_D A_{ref} \rho v^3 \quad (2)$$

where  $C_D$  is the satellite's coefficient of drag,  $A_{ref}$  is the crosssectional area of the satellite projected in the direction of  $v$ , the velocity of the satellite in the ECEF coordinate frame,  $m$  is the satellite mass,  $\rho$  is the mass density. Winds are neglected in this equation, however, the co-rotation of the atmosphere with the Earth is automatically considered through the use of ECEF coordinates. To compute the coefficient of drag, we consider the transfer of momentum between incoming atmospheric particles and the satellite surface assuming that particles are accommodated to the approximate surface temperature of the satellite using an accommodation coefficient of  $\alpha = 0.93$  [8]. This constant accommodation coefficient is an approximation that we will strive to improve in future work.

In order to compare two subsequent observations of orbital energy  $\xi_0$  and  $\xi_1$  calculated by Eq. 1 at their respective epochs  $t_0$  and  $t_1$ , Eq. 2 can be integrated to find the dependence on atmospheric density:

$$\xi_1 - \xi_0 = -\frac{1}{2m} \int_{t_0}^{t_1} C_D A_{ref} \rho v^3 dt = -\frac{1}{2m} \rho_{eff} \int_{t_0}^{t_1} C_D A_{ref} v^3 dt \quad (3)$$

Solving for  $\rho_{eff}$ , similar in theme to the work of [9], gives an effective mass density between  $t_0$  and  $t_1$  along the orbit of the satellite.

Fig. 5 shows the simulated change in orbital energy normalized by neutral density as given by Eq. 2 for one of Spire Global's CubeSats according to its orientation over the course of a single day. This parameter, which we can refer to simply as the force model, is the conversion factor between the observed energy dissipation rate and atmospheric

density. The periodic shift between pointing modes—one optimized for RO sensing and the other for solar panel illumination—can be clearly seen in Fig. 5. Accounting for the large variations in the force model becomes crucial because a satellite can dwell in a given pointing mode for a significant fraction of an orbit, and this dwell time is not necessarily consistent between orbits. If neglected, these approximate factor-of-2 variations in the force model have the potential of causing errors of similar magnitude in the density retrievals.

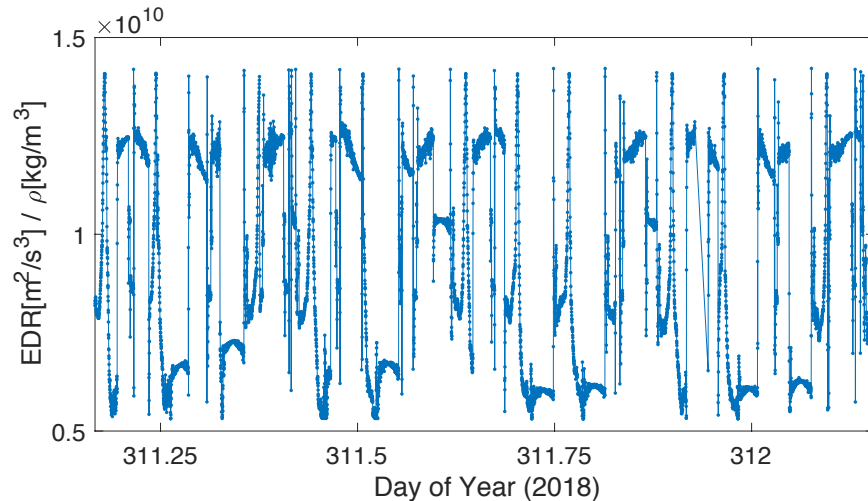


**Fig. 5.** Force model for Spire CubeSat 83 for a single day starting early on 7 Nov. The force model is the conversion factor between the observed energy dissipation rate and atmospheric density.

### 3.4 Driver Estimation & Assimilation

The Iterative Driver Estimation and Assimilation (IDEA) technique is based on the method of [4]. This method accounts for the complex relationship between external drivers—namely solar flux and geomagnetic heating—and the resulting response of the upper atmosphere. In general, these drivers are poorly monitored and often rely on proxies that only very approximately represent the physical mechanisms heating and energizing the upper atmosphere. To represent the absorption of solar extreme and far ultraviolet (EUV/FUV) irradiance, the solar radio flux at 10.7 cm wavelength ( $F_{10.7}$ ) is often used as a proxy. In terms of the solar wind–magnetosphere–ionosphere–thermosphere interaction, the geomagnetic Kp index is often used to characterize heating and momentum exchange at high latitudes. Parameterized coupling functions are then used to convert these proxies into atmospheric heating, incurring further uncertainty into the overall modeling process. The reliance on these proxies and their coupling functions leads to large uncertainties when driving a model of the thermosphere.

IDEA estimates corrections to the external forcing parameters and their coupling functions in order to bring a model into better agreement with direct observations of the thermosphere. The discrepancies between model output and observations are minimized by employing a least-squares filter similar in nature to an unscented Kalman filter (UKF). Fig. 6 compares the IDEA process (right) to that of a typical ensemble Kalman filter (EnKF) configured for ionosphere/thermosphere modeling. IDEA runs several versions of the thermosphere model, each experiencing slightly different external driving conditions.

In the current implementation of IDEA, the Thermosphere–Ionosphere–Electrodynamics General Circulation Model (TIEGCM) [10,11,12] is used as the physics-based environment model. TIEGCM is a finite-difference solution to the conservation equations of momentum, mass, and energy describing the upper atmosphere in the presence of momentum and energy sources. TIEGCM accounts for the dominant features in the upper atmosphere of molecular diffusion and circulation, solar heating in the EUV and FUV bands, and high-latitude auroral heating. TIEGCM also has the ability to simulate the ionosphere and associated electrodynamic coupling between the neutral and plasma environment in a self consistent manner at middle and low latitudes.

In terms of data assimilation, additional measures must be taken to deal with the lagged response of the upper atmosphere to variations in the external drivers. It is well known that the response of the thermosphere can take on a large range of timescales dependent on several factors, height being among the largest contributors. In order for an estimated correction of the external forcing parameters to have a timely effect on the model, the time-lagged response

must be accounted for. IDEA abandons the sequential filtering techniques typically used for ionosphere/thermosphere applications. Instead, an iterative approach is adopted so that estimated forcing parameters can be re-applied to a simulation over the course of one day so that the model can respond to forcing (refer to the additional feedback loop on the right side of Fig. 6).

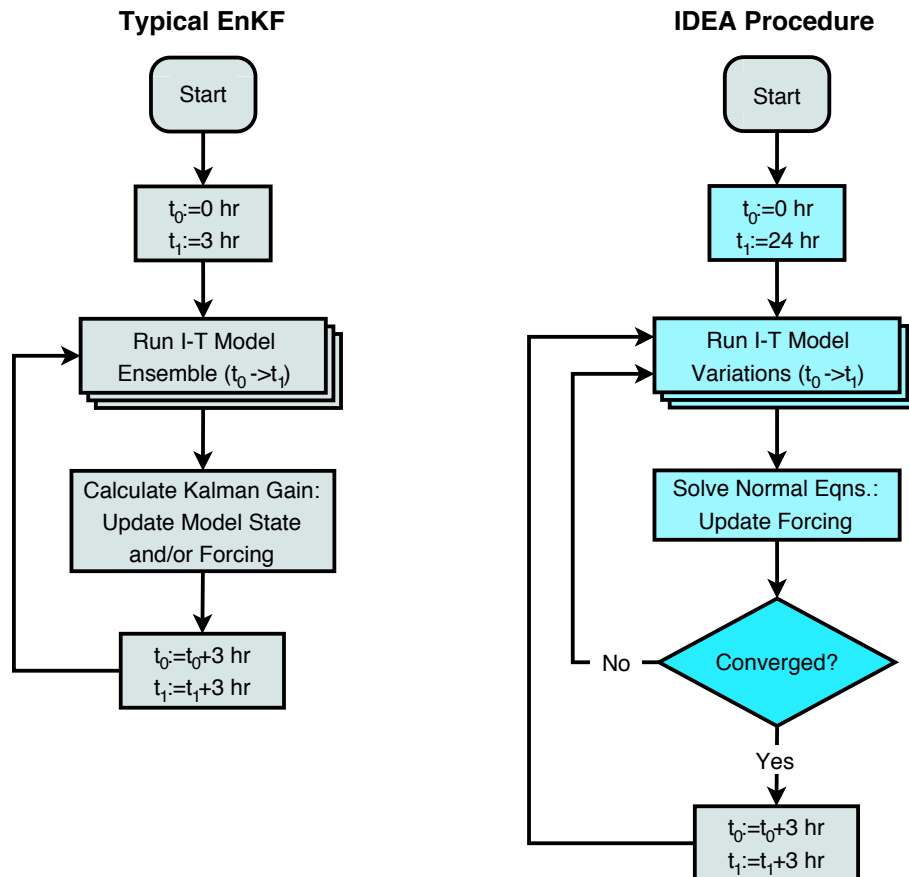


**Fig. 6.** Comparison of a typical Ensemble Kalman Filter as configured for use with a time-dependent thermospheric model (left) with the IDEA technique (right; items in color have been added or modified with respect to the EnKF flow chart), where  $t_0$  and  $t_1$  are the respective start and end times of the model runs during a given data assimilation cycle (from [4]).

In [4], satellite-borne accelerometer observations of thermosphere density were used to calibrate the external forcing parameters driving the TIEGCM. Here we use EDRs based on POD ephemeris derived from GNSS measurements from 3 satellites from Spire Global’s constellation of CubeSats. A forward model, based on output from the TIEGCM, the satellite geometry model shown in Fig. 2, and the force model of [8], is used to synthesize orbital energy dissipation for each satellite according to Eq. 3. Accelerometer data operates at high cadence (0.1–1 Hz) equating to a resolution of 7–70 km along the satellite’s orbit. The GNSS/POD data set yields a measurement of density more on the order of once per orbit arc (possibly higher with additional development). This difference in information content between data sets necessitates additional consideration when designing a thermospheric estimation filter. In this case, we found that the observability of IDEA was limited to estimation of the most recent daily  $F_{10.7}$  value and the most recent 6-hourly effective  $K_p$  value. For comparison, [4] found it possible to estimate the most recent daily  $F_{10.7}$  value and the three most recent 3-hourly  $K_p$  values when using the high-resolution accelerometer-derived density data set. However, it is expected that improvement in observability will be enabled through the use of more CubeSats in the estimation process. And considering the much high coverage of CubeSats in altitude and local time, accuracy could very easily exceed accelerometer-based density model corrections.

#### 4. RESULTS AND DISCUSSION

The period spanning 23 Sept.–9 Dec. 2018 (days 266–343) of our study was marked with very low activity in terms of the magnitude and variation of solar EUV and FUV, as approximated by measurements of the 10.7 cm solar radio flux ( $F_{10.7}$ ; top panel of Fig. 7). Note that  $F_{10.7}$  has an approximate lower bound of 66 solar flux units (sfu) at solar minimum and attains values above 200 during solar maximum. During the latter, 27-day solar rotational modulation can also produce large swings in  $F_{10.7}$  with concomitant signals in the thermospheric density. Because the 2018 period falls firmly within solar minimum, the variations seen here are quite small. In terms of geomagnetic activity, however, there were two minor-to-moderate disturbances on 7 Oct. (day 280) and 4 Nov. (day 308) as shown by the 3-hourly Kp geomagnetic index (lower panel of Fig. 7).

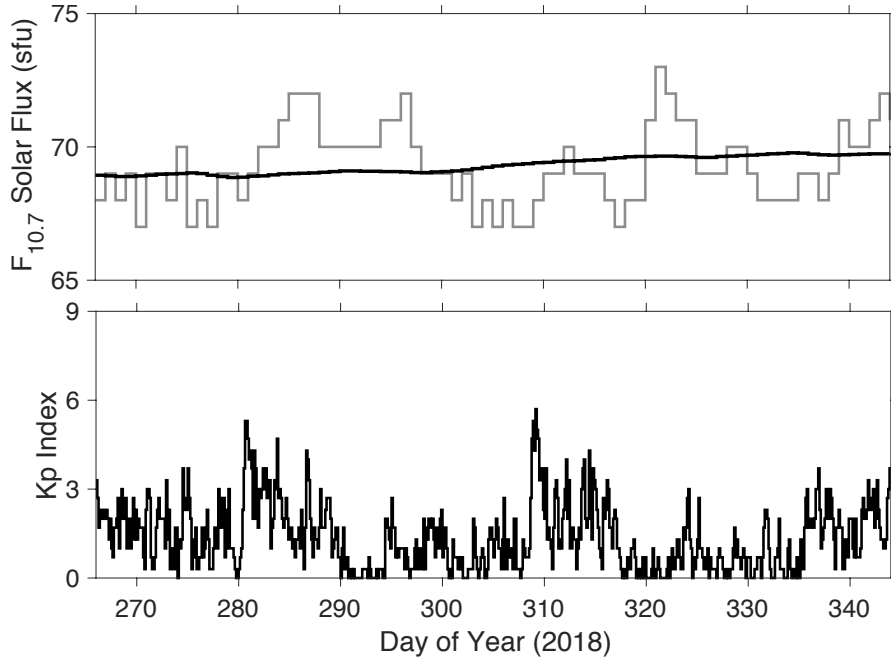


**Fig. 7.** Top: observed solar  $F_{10.7}$  radio flux. The grey curve is the daily measured value from the Ottawa observatory normalized to 1 AU sun-earth distance; the black curve is an 81-day ( $\sim 3$  solar rotation) centered average. Bottom: the 3-hourly planetary magnetic index Kp. Both panels span the period of interest 23 Sept.–9 Dec. 2018.

Given observations of orbital variations and an appropriate force model as discussed in the previous section, an effective atmospheric mass density can be inferred between orbit arcs. Fig. 8 shows such neutral mass densities derived from the three CubeSats (blue, red and yellow curves) of Spire’s constellation. The cadence of these densities is approximately one measurement per orbit arc. For the time period studied, this equates to a cadence of about 2–2.5 hours on average. However, this cadence depends on the instrument duty cycle, which has steadily improved since 2018. HASDM output is also shown with the black curve for reference. This empirical model is calibrated by ground-based radar tracking observations of approximately 70–90 orbiting objects. Because the individual tracking observations are sparse—relative to those available from GNSS—densities derived from this technique have an effective cadence of several hours to several days [3].

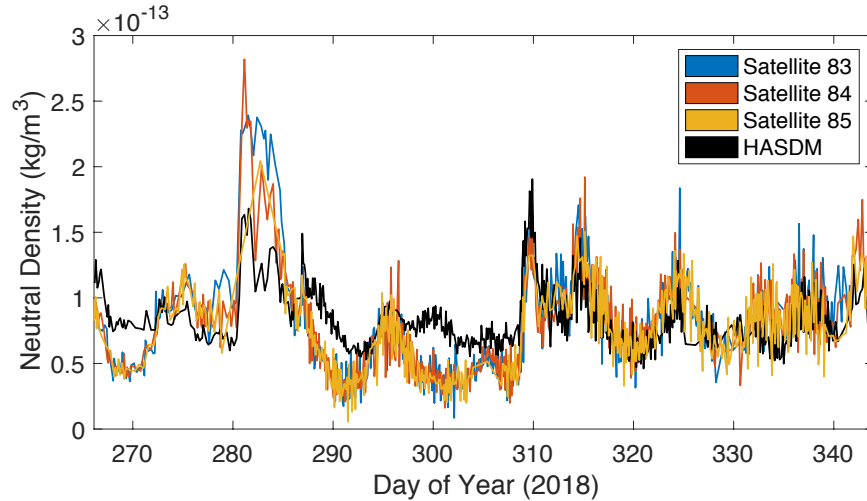


**Fig. 8.** Neutral mass densities derived from Spire CubeSats 83–85. Also shown is output from HASDM as sampled on the orbit of satellite 84. The values plotted are the effective densities (see the right-hand side of Eq. 3) between subsequent orbit arcs.

The CubeSat-derived densities maintain good agreement with one another and reasonable agreement with HASDM. As Fig. 7 shows, there are several minor to moderate variations in  $K_p$  over the time interval. The signatures of these disturbances are also seen in the neutral densities of Fig. 8. There are several deviations between data and model though, most notably around days 270, 290, and 300, where CubeSat-derived densities are significantly lower than HASDM. We have not yet concluded whether model or data are in error during these intervals, since very little ground-truth data exists during this period for validation. Another period of discrepancy exists around the geomagnetic disturbance on day 280, where CubeSat-derived densities experience a much larger storm-time increase. We note that POD data were less frequent during this particular event than during other times. The discrepancy in amplitude during this event could also be a function of the higher cadence of the CubeSat POD data fit spans (5–6 hours during this event) relative to that of the HASDM data fit spans (~1 day or more), in which case, the CubeSat-derived densities would be expected to more accurately resolve the storm-time disturbance.

A central goal of this work is to ingest multiple data sources into a physic-based, assimilative thermosphere model to combine information and mitigate the uncertainty of any one dataset. Fig. 9 shows the baseline TIEGCM simulation without any assimilation (grey curve) driven externally by the observed geophysical indices (GPI) of  $K_p$  and  $F_{10.7}$ ; the POD-based densities derived using the techniques described in the previous Section (blue, red, and yellow curves); and the IDEA output over the interval spanning 23 Sept.–9 Dec. 2018 (solid black curves).

The baseline TIEGCM-GPI simulation shows muted response to the  $K_p$  and  $F_{10.7}$  inputs during this interval, when compared with the IDEA output (or with the HASDM output in Fig. 8). CubeSat densities and IDEA output agree very well over the interval. There are, however, several short periods during which data from a single satellite becomes sparse, such as the period around day 304–306 for satellite 85 (yellow curve). There are also several periods during which data from a single satellite becomes spurious, not agreeing with the data from the other two satellites, such as the period around 335–340 for satellite 85 (yellow curve). In both cases, the other two data sets tend to compensate for missing or spurious data from the third satellite. This leads us to believe that adding data from additional satellites and constellations should improve performance and increase the "signal-to-noise ratio" of the data assimilation process.

The performance of these models with respect to the CubeSat-derived densities are assessed using the metrics of [4]. These are essentially the mean ( $\mu$ ), standard deviation ( $\sigma$ ), and root mean square error ( $RMSE$ ) of the ratio of model density to observed density:

$$\mu(m/o) = \exp\left(\frac{1}{N} \sum_{i=1}^N \ln \frac{\rho_{m,i}}{\rho_{o,i}}\right) \quad (4)$$

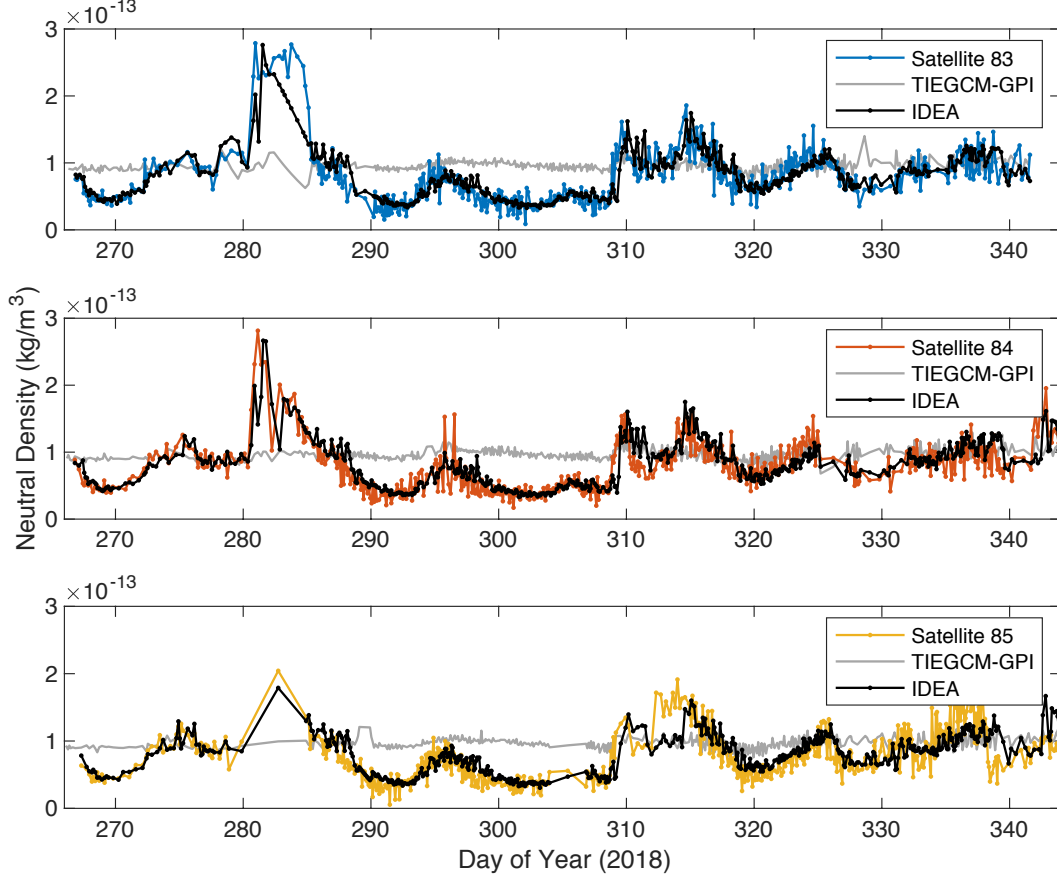


**Fig. 9.** Comparison of observations with model output. CubeSat-derived densities are given by the colored curves for satellites 83 (top), 84 (middle), and 85 (bottom). Also shown is the output from the baseline thermosphere model driven by measured geophysical indices (TIEGCM-GPI, grey curves)  $F_{10.7}$  and  $K_p$ . The data assimilation IDEA output is given along each of the CubeSat orbits by the black curves.

$$\sigma(m/o) = \sqrt{\frac{1}{N} \sum_{i=1}^N \left( \ln \frac{\rho_{m,i}}{\rho_{o,i}} - \ln \mu(m/o) \right)^2} \quad (5)$$

$$RMSe(m/o) = \sqrt{\frac{1}{N} \sum_{i=1}^N \left( \ln \frac{\rho_{m,i}}{\rho_{o,i}} \right)^2} \quad (6)$$

As mentioned in [4], these metrics have several properties that are desirable when working with the ratio of a quantity, such as neutral density, that varies exponentially. The  $RMSe(m/o)$  and  $\sigma(m/o)$  quantities are best interpreted as a percentage in the following way:  $\% = 100 \times (\exp \sigma(m/o) - 1)$ . The  $RMSe(m/o)$  is a combination of  $\mu(m/o)$  and  $\sigma(m/o)$ , as can be seen through the following relation:  $RMSe(m/o)^2 = (\ln \mu(m/o))^2 + \sigma(m/o)^2$ . The  $RMSe(m/o)$  is therefore a good indicator of total model errors. However, if the intent is to drive a POD process using the density model, it may be more informative to use the  $\sigma(m/o)$  metric, since a ballistic coefficient is typically estimated per satellite. In practice, this estimated ballistic coefficient will soak up errors not only in the assumed coefficient of drag, but also in the mean bias of the density model. Table 2 shows the overall performance of the three models, TIEGCM-GPI, HASDM, and IDEA at recreating the Spire CubeSat data.

During the period of interest, the IDEA method clearly outperforms HASDM in all three metrics. This is true of both the prior and posterior IDEA estimates of density; the former is a 6-hour persistence forecast of the external drivers while the latter is the fully assimilated solution. It should be noted, however, that IDEA has a clear advantage over the other two models in this comparison, since IDEA assimilates the very data that it is now being validated against. This

scenario is somewhat unavoidable, as there is currently a lack of independent validation data sources related to neutral density. Because of this situation, any systematic errors in our data processing or underlying assumptions are not expected to be revealed by this comparison and validation. Instead, our findings are that the IDEA technique, as an estimation filter, has the requisite control authority to sufficiently adjust the model to the assimilated data set.

**Table 2.** Performance metrics of each model with respect to the assimilated Spire Global CubeSat data, calculated over the entire interval spanning days 266–343, 2018.

	TIEGCM-GPI	HASDM	IDEA	
			Prior	Posterior
$\mu(m/o)$	1.37	1.14	1.06	1.06
$\sigma(m/o)$	58.6%	51.7%	38.5%	33.9%
$RMSe(m/o)$	75.1%	55.0%	39.3%	34.7%

## 5. SUMMARY AND CONCLUSIONS

The increasing crowdedness of the satellite and debris populations in LEO necessitates improvements in how we detect, track, and catalog orbiting objects. Additionally, if we are to avoid catastrophic collisions in LEO, we must also be able to reliably predict the trajectories of satellites multiple days in advance. With the variability of the space environment, particularly thermospheric mass density, being the largest uncertainty in the orbit prediction chain, this study investigates new ways to monitor the upper atmosphere. In this notoriously data-starved region, the instrumentation commonly carried on recently launched LEO SmallSats and CubeSats, particularly GNSS receivers, can provide essential corrections to physics-based models of the thermosphere. Notably, the amount of data available from this new category of observation should continue to scale with the crowdedness of LEO, whereas the current ground-based tracking database remains limited in quantity and resolution.

In the current work, we have applied a post-processing method to the timeseries of POD ephemeris from three CubeSats in Spire’s constellation. This has allowed us to track the orbital energy of each CubeSat over time. Further application of a satellite-surface force model allows us to relate the time evolution of orbital energy to the *in situ* atmospheric mass density. While the resulting timeseries from a single satellite may be prone to errors, identified here simply as a discrepancy between density timeseries derived from co-orbiting CubeSats, this can be mitigated by assimilating timeseries from multiple data sets into a physics-based model of the thermosphere.

With more advanced processing methods, it may be possible to lower the noise for timeseries of individual CubeSats. Moreover, it may also be possible to attain higher cadences than a single data point per orbit. In fact, this has already been demonstrated when using the state-of-the-art geodetic GPS receiver [7]. When paired with a suitable assimilative, physics-based models of the thermosphere, there is great potential to lower uncertainty across the LEO catalog, improve the accuracy of conjunction assessments, and increase the efficacy of Space Traffic Management (STM) activities.

## 6. REFERENCES

- [1] Sutton, E. K., Forbes, J. M., and Nerem, R. S. (2005), Global thermospheric neutral density and wind response to the severe 2003 geomagnetic storms from CHAMP accelerometer data, *J. Geophys. Res.*, 110, A09S40. <https://doi.org/10.1029/2004JA010985>.
- [2] Krauss, S., M. Temmer, A. Veronig, O. Baur, and H. Lammer (2015), Thermospheric and geomagnetic responses to interplanetary coronal mass ejections observed by ACE and GRACE: Statistical results, *J. Geophys. Res. Space Physics*, 120, 8848–8860. <https://doi.org/10.1002/2015JA021702>.
- [3] Storz, M. F., Bowman, B. R., Branson, M. J. I., Casali, S. J., & Tobiska, W. K. (2005). High accuracy satellite drag model (HASDM), *Advances in Space Research*, 36, 2497–2505. <https://doi.org/10.1016/j.asr.2004.02.020>.
- [4] Sutton, E. K. (2018). A new method of physics-based data assimilation for the quiet and disturbed thermosphere. *Space Weather*, 16, 736–753. <https://doi.org/10.1002/2017SW001785>.
- [5] Reigber, Ch., Schwintzer, P., Neumayer, K.-H., Barthelmes, F., König, R., Förste, Ch., Balmino, G., Biancale, R., Lemoine, J.-M., Loyer, S., Bruinsma, S., Perosanz, F., Fayard, T. (2003), The CHAMP-only Earth Gravity Field Model EIGEN-2. *Advances in Space Research*, 31(8), 1883–1888. [https://doi.org/10.1016/S0273-1177\(03\)00162-5](https://doi.org/10.1016/S0273-1177(03)00162-5).
- [6] Hedin, A. E. (1991), Extension of the MSIS Thermosphere Model into the middle and lower atmosphere, *J. Geophys. Res.*, 96(A2), 1159–1172. <https://doi.org/10.1029/90JA02125>.
- [7] van den Ijssel, J., & Visser, P. (2007), Performance of GPS-based accelerometry: CHAMP and GRACE, *Advances in Space Research*, 39, 1597–1603. <https://doi.org/10.1016/j.asr.2006.12.027>.
- [8] Sutton, E. K. (2009), Normalized Force Coefficients for Satellites with Elongated Shapes, *J. Spacecraft and Rockets*, 46(1), 112–116. <http://doi.org/10.2514/1.40940>.
- [9] Picone, J. M., J. T. Emmert, and J. L. Lean (2005), Thermospheric densities derived from spacecraft orbits: Accurate processing of two-line element sets, *J. Geophys. Res.*, 110, A03301. <https://doi.org/10.1029/2004JA010585>.
- [10] Richmond, A. D., Ridley, E. C., & Roble, R. G. (1992). A thermosphere/ionosphere general circulation model with coupled electrodynamics. *Geophysical Research Letters*, 19, 601–604. <https://doi.org/10.1029/92GL00401>.
- [11] Qian, L., Burns, A. G., Emery, B. A., Foster, B., Lu, G., Maute, A., et al. (2014). The NCAR TIE-GCM: A Community Model of the Coupled Thermosphere/Ionosphere System. *Geophysical Monograph Series 201* (pp. 73–83). Washington, DC: Geopress, American Geophysical Union. <https://doi.org/10.1002/9781118704417.ch7>.
- [12] Sutton, E. K., Thayer, J. P., Wang, W., Solomon, S. C., Liu, X., & Foster, B. T. (2015). A self-consistent model of helium in the thermosphere. *Journal of Geophysical Research: Space Physics*, 120, 6884–6900. <https://doi.org/10.1002/2015JA021223>.